# Differential cross sections for rotationally inelastic scattering of NO from He and $D_2$

M. S. Westley
*Department of Applied and Engineering Physics, Cornell University, Ithaca, New York 14853-1301*

K. T. Lorenz and D. W. Chandler
*Combustion Research Facility, Sandia National Laboratories, Livermore, California 94550*

P. L. Houston[a)]
*Department of Chemistry and Chemical Biology, Cornell University, Ithaca, New York 14853-1301*

(Received 21 September 2000; accepted 14 November 2000)

State selective differential cross sections for rotationally inelastic scattering of NO ($J_i=0.5$, 1.5, $F_1 \rightarrow J_f=2.5-12.5$, $F_1$ and $J_f=1.5-9.5$, $F_2$) from He and $D_2$ measured by crossed molecular beam product imaging are reported. The differential cross sections were extracted from the data images using a new basis image iterative fitting technique. The images typically exhibit a single broad rotational rainbow maximum that shifts from the forward to the backward scattering direction with increasing $\Delta J$. The angle of the rainbow maximum was lower at a given $\Delta J$ for $D_2$ than for He as a collision partner. At a collision energy of $\sim 500\ cm^{-1}$, primarily the repulsive part of the potential surface is probed, which can be modeled with a two-dimensional hard ellipse potential. This model for rotationally inelastic scattering is shown to qualitatively match the experimental differential cross sections. A more advanced correlated electron pair approximation potential energy surface for NO+He does not give substantially better agreement with the experiment. The differences between scattering of He and $D_2$ are partially attributed to their differing structure and partially to a small difference in collision energy used in the two experiments. © *2001 American Institute of Physics.* [DOI: 10.1063/1.1338528]

## I. INTRODUCTION

Rotationally inelastic scattering of molecules is of fundamental importance in energy transfer of molecular gases. Integral and differential cross sections for rotationally inelastic scattering of NO from collisions partners such as He, Ar, NO, and $N_2$ have been extensively studied. Along with these experimental studies, potential energy surfaces (PES) for NO–Ar and NO–He have been generated and tested against experimental results. The sheer volume of theoretical and experimental work done on NO is attributable to several factors. First, NO is experimentally convenient; it is one of the few radical species that is stable enough to be stored in a gas cylinder. Next, the spectroscopy of NO makes it very sensitive to laser-based detection methods such as resonantly enhanced multiphoton ionization (REMPI) or laser-induced fluorescence (LIF). Finally, NO is of theoretical interest, partially because of the extensive experimental work that has been done, but also because NO is a radical species with nonzero orbital angular momentum in its ground state, which gives rise to complex potential interactions.

Some early measurements of collision-induced energy transfer in NO were carried out in a bulb using laser-based resonance techniques. For example, Subdo and Loy used an IR UV double resonance (IRUVDR) technique to measure integral cross sections for rotationally inelastic and spin–orbit conserving and changing collisions of NO($v=2$) with NO, He, Ar, $N_2$, CO and $SF_6$.[1,2] More recently, Islam *et al.* have performed studies of integral state–state cross sections using IRUVDR for NO($v=2$) scattering with He, Ar, and $N_2$ and compared their results with the latest theoretical predictions.[3] Other recent studies have used the IRUVDR technique to look at rotational energy transfer of NO (colliding with He, Ar, and $N_2$) at the exit of a Laval nozzle, a specially shaped nozzle that produces a flow of gas at a constant low temperature and pressure over several centimeters.[4] The experimental data were found to be in excellent agreement with the latest theoretical calculations.

Measurements of integral cross sections for NO scattering have also been performed using a crossed molecular beam technique. The rotational cooling of the molecular beam expansion produces rotationally cooled NO (typically >90% in $J=0.5$, in $F_1$, the lower spin–orbit state, with equal $\Lambda$ doublet populations) and laser-based probe techniques can be used to examine specific final states of NO (including final $\Lambda$ doublet level, depending on which branch is used to ionize the NO). Also, collisions which cause the NO to change from the ground spin–orbit state to the upper spin–orbit state are routinely investigated. The pioneering work by Joswig, Andresen, and Schinke used fixed molecular beams and LIF detection of NO after colliding with Ar, Ne, and He.[5] Cross sections for $F_1 \rightarrow F_1$ scattering have been measured or predicted to be 5–10 times larger than those for $F_1 \rightarrow F_2$ scattering.[6,7] These studies have also observed that the integral cross sections, in general, decrease in magnitude with increasing $\Delta J$.[8] Additionally, several experiments have

a)Electronic mail: plh2@corncll.edu

 

observed Λ doublet propensities in integral cross sections for spin–orbit conserving and changing collisions for NO+Ar.[9,10]

Crossed molecular beam techniques combined with rotatable detectors (or a fixed detector and rotatable beams) provide a method for measuring the differential cross section for NO scattering. Using electron impact ionization to detect He scattering from NO, Keil *et al.* were able to accurately measure diffraction oscillations of the scattered He and thus model the attractive part of the NO–He potential.[11] Thuis *et al.* used a hexapole selection technique and molecular beams to examine the angle dependence of scattering by specific spin–orbit states of aligned NO in the late 1970s.[12,13] Gentry and co-workers used crossed, rotatable molecular beams and a laser ionization time-of-flight (TOF) detector to record integral and differential cross sections for NO scattering from Ar, NO, CO, and $O_2$.[7,10,14,15] Wodtke and co-workers made detailed integral cross-section measurements of rotationally inelastic scattering of vibrationally excited NO using a crossed beam technique.[16] They found that the integral cross sections could be predicted by considering the vibrationally excited NO to have an extended bond length corresponding to the equilibrium bond length in the vibrationally excited state. Meyer used counterpropagating molecular beams, a TOF detector, and (2+1) REMPI through the $E\,^2\Sigma^+$ state of NO to make measurements of the differential cross sections, integral cross sections, and alignment of NO scattering from He.[17] Meyer found differences in rotational rainbow structure for spin multiplet changing versus conserving collisions which he attributed to differences in the anisotropy for the two processes using a hard ellipse model. He also observed oscillations in integral cross sections superimposed on an overall decline in cross section with $\Delta J$ well modeled by an energy gap law, and alignment of the scattered NO that could be explained by a geometric apse model.[18–21]

NO is an interesting candidate for theoretical study because it has a $^2\Pi$ ground state. A NO molecule has two nearly degenerate Λ doublet levels that represent, in the limit of high *J*, the orientation of the *p* orbital of an electron with respect to the rotation vector. The approach of another species to the NO, breaks the symmetry of these two orbital orientations. Thus, two potential energy surfaces, the $A'$ and $A''$ surfaces, are needed to adequately describe the interactions of NO with another species. The challenge of this problem has made it appealing to theorists. An *ab initio*, electron gas model for NO+Ar was constructed by Nielson *et al.* in the late 1970s.[22] This surface was used by Meyer (with a change in the reduced mass of the system to make it appropriate for NO+He) to model his differential and integral cross-section measurements.[17] A more detailed theory for the interactions between atoms and molecules in II electronic states was formulated by Alexander in 1984.[23] Using this theoretical framework and a CEPA (correlated electron pair approximation) *ab initio* based method, Alexander produced a PES for NO+Ar.[6] A NO+He PES based on this NO+Ar PES has also been produced by Yang and Alexander and results from the NO+He surface are in good agreement with the differential and integral cross-section data of Meyer.[17,24] The latest PESs are available for use for the general scientific community through the use of a numerical package called HIBRIDON™, which was used in this report to generate differential cross sections for NO+He. No PES for NO+$D_2$ is known to be presently available.

Imaging techniques, combined with crossed molecular beams and state selective ionization, provide an effective tool for measuring angular distributions from rotationally inelastic scattering. NO scattering from Ar was first imaged by Houston and co-workers, but since then improvements have been made on the technique.[25,26] They observed two rotational rainbows for NO+Ar scattering, and no pronounced difference in differential cross sections for spin multiplet changing versus spin multiplet conserving collisions. The use of velocity mapping and ion counting for imaging scattering reactions has recently been shown to produce remarkable results.[27] The measurements reported here are part of a series of rotationally inelastic scattering studies using a new crossed beam imaging apparatus at Sandia National Laboratory (the other systems studied include HCl+Ar and CO+Ne[28,29]).

This work represents an effort to compare differential cross sections of NO scattering with two different species having approximately the same mass, He and $D_2$. The state-selective detection of NO scattering from a light collisional partner requires good angular resolution of slow lab-frame scattering products. This resolution has only recently been possible due to the advancements in velocity mapping of product ions.[30] The imaging technique for molecular scattering lends itself to easy qualitative interpretation of angular distributions. However, for accurate quantitative information, substantial analysis of the images must be performed. This article describes one method for performing this analysis, while other, very similar, methods have been described in recent work.[28,29] The focus of this work was to collect a series of differential cross sections as a function of $\Delta J$ for spin multiplet conserving ($F_1 \rightarrow F_1$) and spin multiplet changing ($F_1 \rightarrow F_2$) scattering events. We also wished to compare the effect of having different scattering species, an atom versus a diatomic molecule, under very similar experimental conditions. Therefore, every effort was taken to minimize laser-dependent alignment effects. Furthermore, because the strength of the imaging apparatus is the measurement of angular distributions, and because integral cross sections for NO scattering have been measured previously, integral cross sections are not reported. Instead, the relative differential cross sections (which can be scaled by previously reported integral cross-section data) for rotationally inelastic scattering of NO ($J=0.5$, $F_1$)+X→NO($J=2.5-12.5$ $F_1$ or $J=1.5-9.5$, $F_2$)+X, where X is either He or $D_2$, are reported in the following.

## II. EXPERIMENT

The spin multiplet conserving scattering experiments were performed in a crossed molecular beam laser ionization ion imaging apparatus at the Combustion Research Facility at Sandia National Laboratory, which was described in detail in an earlier report.[28] The spin multiplet changing experiments were performed in a very similar apparatus at Cornell

University.[31] In each apparatus, two molecular beams are generated in differentially pumped source chambers, pass through collimating apertures, and intersect in an interaction chamber capable of maintaining a pressure of $7\times10^{-7}$ Torr with both molecular beams pulsed at 30 Hz. The products of the scattering reaction are state-selectively ionized in the interaction region by a focused, pulsed probe laser. At the intersection region of the main chamber, a set of ion lenses mounted perpendicular to the plane of the molecular beams extract and focus[30] the ions through a time-of-flight mass spectrometer (TOFMS) and onto a position sensitive microchannel plate (MCP)/phosphor detector. The phosphor is imaged by a charge-coupled device (CCD) camera and the signal is integrated over a succession of shots either on the CCD chip or in a computer.

For both sets of experiments, a 2% NO in argon mixture was used for the NO molecular beam, while a neat expansion of $D_2$ or He was used for the scattering beam. The backing pressure behind each expansion was typically around 2 atm. The distribution of molecular or atomic velocities in each of the beams could be measured by using the image of each molecular beam, the known flight time of the ions through the TOFMS, and the measured magnification of the ion optics. For measurement of the velocity distribution of the He scattering beam, a trace amount of NO was added to the gas to obtain the velocity distribution image. The velocity profile of the $D_2$ beam was measured by ionizing the $D_2$ directly using 2+1 REMPI with 204–205 nm light through the $E,F$ state.[32] The resulting velocity distributions are well modeled by Gaussian profiles with the following characteristics: $v_{\mathrm{He}}=1730$ m/s, full width at half maximum (FWHM)-80 m/s $v_{\mathrm{D_2}}=1834$ m/s, FWHM-230 m/s; $v_{\mathrm{Ar/NO}}=574$ m/s, FWHM=62 m/s. These velocities are consistent with an isentropic beam expansion through a nozzle at a temperature of approximately 310 K. In order to extract absolute numbers for the above-mentioned velocity distributions, it is necessary to know the magnification factor of the ion optics. The magnification factor was measured by least-squares fitting the diameters of the Newton spheres for scattering into different final rotational levels of NO.[28] The results of this fitting give collision energy for the NO+He system of 491 $\mathrm{cm}^{-1}$ (with a FWHM of 42 $\mathrm{cm}^{-1}$) and a collision energy of 545 $\mathrm{cm}^{-1}$ (with a FWHM of 125 $\mathrm{cm}^{-1}$) for the NO+$D_2$ system.

The state distributions of the $D_2$ and NO in the molecular beams were also measured. Due to the large energy spacing of the rotational levels of $D_2$ and the *ortho–para* selection rules for $J$ changing collisions in $D_2$, the rotational degrees of freedom of $D_2$ in the molecular beam expansion are not in equilibrium. Therefore, the ratio of specific heats, $\gamma$, for the molecular beam expansion of $D_2$ is between the limits of 5/3 (for no rotational degrees of freedom) and 7/5 (for the two rotational degrees of freedom of a diatom). Furthermore, the populations of $D_2$ in the beam are not thermally distributed, and were directly measured by 2+1 REMP1[33] to be 38%, 35%, 22%, and 5% in $J=0-3$, respectively, with the population in $J>3$ less than 1%. The rotational distribution of NO in the molecular beam can be extracted from an ionization spectra of the NO and corresponds to a rotational temperature of about 2.5 K. This corresponds to 92% of the NO in $J=0.5$, 8% of NO in $J=1.5$, and less than 1% in $J>1.5$.

For the scattering measurements, NO ionization was effected by lightly focusing the output of frequency doubled YAG pumped dye laser (Sandia apparatus) or a XeCl excimer pumped dye laser (Cornell apparatus) to obtain approximately 1 mJ/pulse of 225–227 nm light. The wavelength range corresponds to 1+1 REMPI through the $A\,^2\Sigma^+$ state of NO. $P$ and $R$ transitions were used to ionize the NO scattered into higher rotational states of the $F_1$ or $F_2$ spin multiplets by collisions with the scattering beam. For $F_1\rightarrow F_1$ scattering, product molecules for $J_f=2.5-5.5$ were detected by use of the $P_{11}$ branch, $J_f=6.5-9.5$ were detected using the $R_{21}$ branch, and $J_f>9.5$ were detected using the $R_{11}+Q_{21}$ branch. The $\Lambda$ doublets probed by this choice of transitions for detection is as follows: $P_{11}:\Pi(A')$ or $e$; $R_{21}:\Pi(A'')$ or $f$; and $R_{11}+Q_{21}:\Pi(A')$ or $e$.[34] For $F_1\rightarrow F_2$ scattering, all of the transitions were probed using the $R_{21}$ branch, which detects $\Pi(A')$ or $e$ $\Lambda$ doublets. The choice of a relatively high power probe laser, 1+1 (as opposed to 1+1′) REMPI, and $P$ and $R$ transitions of NO were made to minimize the possible preferential ionization of NO due to any correlation of rotational alignment and laser polarization. Additionally, because the measured product states are primarily low $J$ states, we expect the rotational alignment of the product NO to be small. The data images were observed to be independent of probe laser polarization direction for the above-mentioned conditions. The images were also insensitive to the particular transition used to ionize the NO for $F_1$, $J_f=4.5$, 7.5, and 10.5, which implies that no differences due to final $\Lambda$ doublet level were observed in the differential cross sections within experimental error. Note, however, that the images presented in the following represent different final $\Lambda$ doublet levels, depending on which $J_f$ was probed.

The NO product ions were extracted from the interaction region by a set of ion optics which focuses the ions with a given velocity projection in the molecular beam plane to the same point on the MCP detector, regardless of starting position of the ion. Due to the fact that the scattering sphere for NO scattering from He or $D_2$ is very small, the voltages used to extract the ions were set as low as possible to maximize the spatial extent of the scattering signal on the MCP. Setting the repeller voltage to 850 V extended the flight time of the NO ions so that the NO product ion scattering sphere for a typical scattering image was 50–60 pixels (5–6 mm) in diameter. The small spread in the lab frame velocity distribution of the scattered NO also meant that the laser bandwidth was sufficient to cover the entire Doppler spread of scattered products with relatively equal laser intensity. The data images, collected by the CCD camera, are the result of subtracting an image with the scattering beam on from an image with the scattering beam off. This subtraction procedure is used to correct for the background population of any high J levels present in the molecular beam expansion.

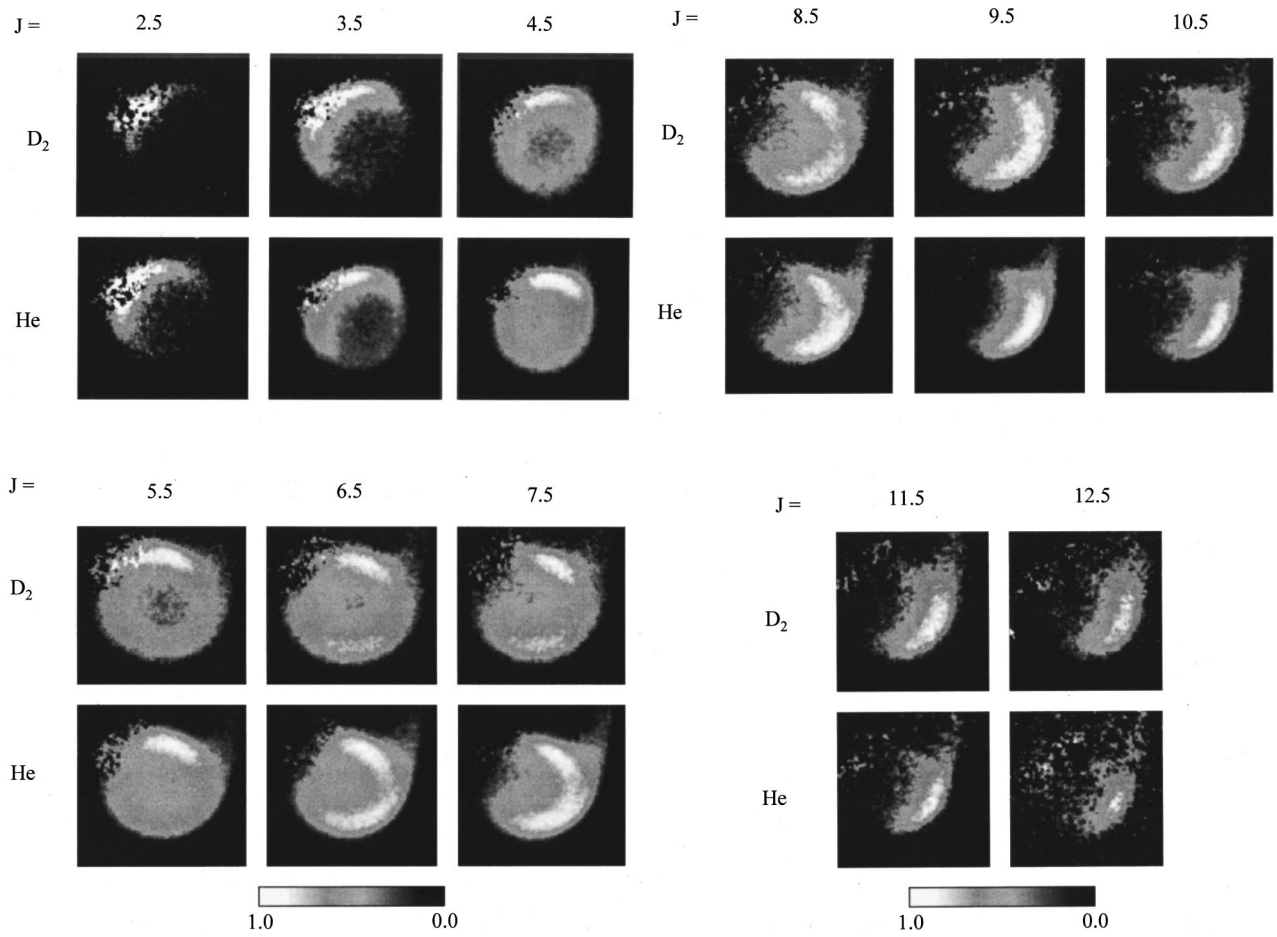


FIG. 1. Ion images for $F_1 \rightarrow F_1$ scattering of NO ($J_i = 0.5,1.5$) with $D_2$ or He into a final rotational level as labeled above.

## III. RESULTS

### A. Image data

The background subtracted ion images for $J_i \sim 0.5$, $F_1 \rightarrow J_f = 2.5-12.5$, $F_1$ are shown in Fig. 1. The images for $J_i \sim 0.5$, $F_1 \rightarrow J_f = 1.5-9.5$, $F_2$ are shown in Fig. 2. Forward scattering intensity appears in the upper left-hand portion of the scattering sphere, while backward scattering intensity appears in the lower right-hand section of the scattering sphere. In order to orient the reader, a Newton diagram for the system is overlaid on the image for NO ($J_f = 5.5$, $F_1$) [Fig. 3(a)]. Qualitative interpretation of the images leads to the conclusion that there is a single broad peak that moves from forward to backward scattering with increasing $\Delta J$ as previously observed for NO–He and NO–Ar inelastic scattering.[10,17,25,26] Additionally, we observe that, for a given $J$, the position of the rainbow maximum is slightly more in the forward direction for $D_2$ than for He.

### B. Image characteristics

There are three major characteristics in the raw images that must be understood and modeled if we are to obtain quantitative differential cross sections (DCSs) from the data: a region of low signal to noise in the net image due to a localized peak in the background intensity, a lab velocity bias in detection efficiency, and a breakdown of the ion optics for ions at the edge of the detection region. These characteristics are illustrated by Fig. 3(b).

The first characteristic is that a region of low signal-to-noise ratio in the forward scattered portion of the images is seen due to background NO in high $J$ levels present in the molecular beam expansion. Even though the beam population of NO in $J > 1.5$ is less than 1%, there is a measurable amount (compared to the intensity of scattered NO) of NO in the molecular beam in $J = 2.5-12.5$. The ion signal from this NO is localized in the image in a region that corresponds to forward scattering. This region of the image thus has a much smaller signal-to-noise ratio than the rest of the image because the net signal is obtained by subtracting two large numbers. This problem is analogous to the problem that crossed beam, rotatable detector experiments experience in the measurement of small angle scattering intensity.

The second characteristic is a velocity-dependent detection bias due to the laser-based method of detection. Scattering should exhibit cylindrical symmetry about the relative velocity vector of the system (unless there is preferential molecular alignment before the collision). However, as can be seen from Fig. 3, the intensity of scattering toward the zero lab velocity side of the image (upper right-hand portion) is higher than that on the high lab velocity side (lower left-hand portion). Collisions of NO occur for tens of microsec-

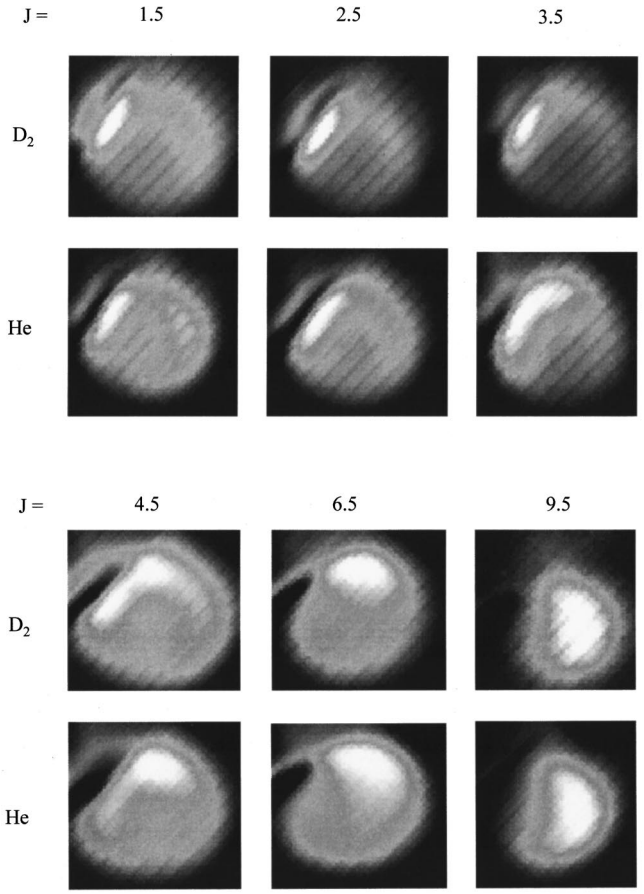


FIG. 2. Ion images for $F_1 \rightarrow F_2$ scattering of NO ($J_i = 0.5, 1.5$) with $D_2$ or He into a final rotational level as labeled above.

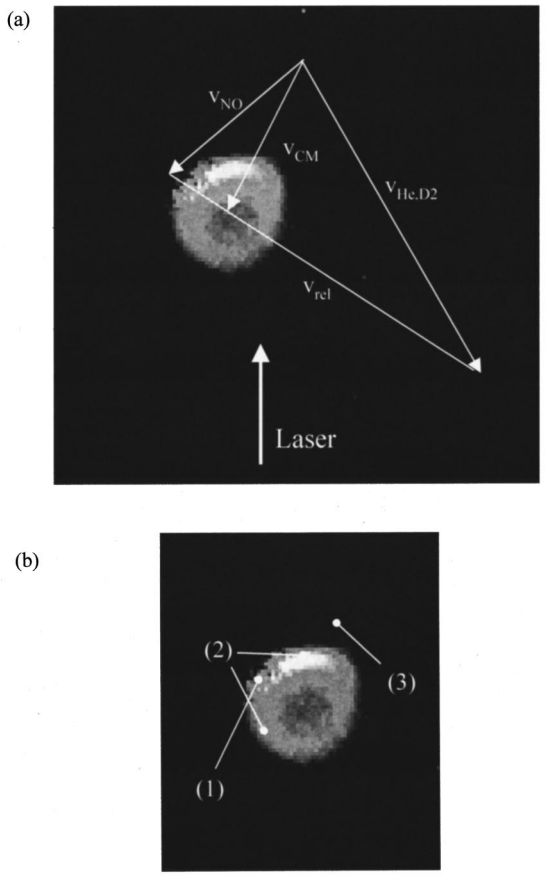


FIG. 3. (a) Typical image, with beam and center of mass velocities superimposed. (b) The characteristics labeled in the image are labeled 1–3: (1) low signal/noise region due to molecular beam background, (2) intensity skew across cylindrical symmetry axis due to velocity detection bias, and (3) nonvelocity mapped ions from edges of detection region.

onds (the gas pulses are 100–200 $\mu$s wide) before the laser passes through the intersection of the molecular beams. The population of scattered NO with different lab velocities in the laser ionization volume is directly related to the lab velocity of the NO. NO with small lab velocities or lab velocities parallel to the laser direction leave the laser ionization volume at a much slower rate than scattered NO with high lab velocities or velocities perpendicular to the laser direction. Thus, there is a preferential detection of scattered NO with small lab velocities or lab velocities parallel to the laser direction. Therefore, although the scattering is symmetric about the relative velocity vector in the center of mass frame, the laser-based detection scheme destroys this cylindrical symmetry about the relative velocity vector in the data images.

The final characteristic in the data images is the ion signal outside of the Newton sphere that trails off to the upper right-hand side. It was hypothesized that these ions were due to scattered NO ionized outside the effective focusing region of the ion optics. This hypothesis was confirmed through the use of a Monte Carlo simulation of the experiment which incorporated a finite difference model of the electric fields in the ion optics. Figure 4 shows a simulated image from this Monte Carlo program and the corresponding data image.

### C. Image simulation

The extraction of an angular distribution from an ion image can be accomplished by various indirect and direct inversion procedures. Notably, for photodissociation experiments and a few crossed beam experiments, an inverse Abel

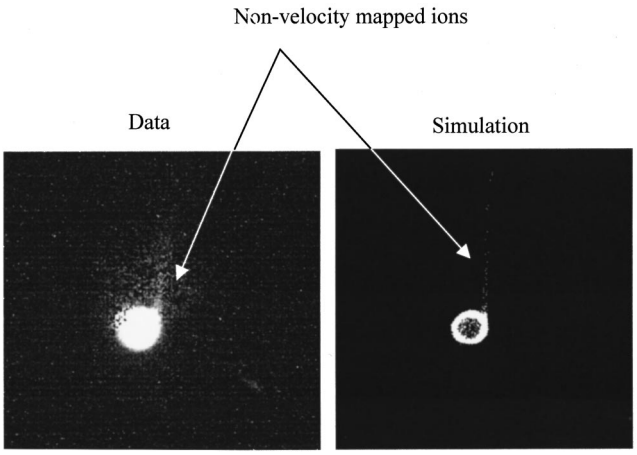


FIG. 4. (a) Monte Carlo simulation of $J_f = 5.5$, isotropic distribution, showing nonvelocity mapped ions trailing off toward top of image. (b) Data, $J_f = 5.5$, He.

transform has been used to extract an angular distribution. However, primarily due to the nonuniform blurring of the scattering intensity across its axis of symmetry, the use of the Abel transform to extract the differential cross sections from the images in this experiment is not appropriate. A rigorous analytical inversion for a crossed beam scattering apparatus is quite difficult and has not, to the authors' knowledge, been developed. Instead, iterative forward simulation is typically used to extract the differential cross section.

The forward simulation process requires the evaluation of at least a nine-dimensional integral to convert the one-dimensional differential cross section into a two-dimensional simulated image. Assuming (1) that there is no angular divergence in the molecular beams, (2) that the velocity mapping is ideal, and (3) that there is no preferential ionization of NO based on alignment relative to the ionization laser polarization, it is necessary to evaluate the following integral:

$$I(\mathbf{x}_I) = \int_{\text{molec}} \int_{\text{beam}} dv_1\, dv_2 \int_{\text{scat vol}} d\mathbf{x}_s \times \int d\mathbf{v}_p \int_{t_s}^{t_L} dt\, N_{\text{MB}}(v_1, v_2, \mathbf{x}_p, t) I_L(\mathbf{x}_p) \times g \frac{\partial \sigma}{\partial \Omega} f_t(\mathbf{v}_p, \mathbf{x}_p, \mathbf{x}_{\text{im}}), \quad (1)$$

where $\mathbf{x}_p = \mathbf{x}_s + (\mathbf{v}_p + \mathbf{v}_{\text{c.m.}})(t - t_s)$, where $\mathbf{x}_I$ is the two-dimensional (2D) pixel position, $v_1$, $v_2$ are the speeds of the radical (NO) and scattering beam, $\mathbf{x}_s$ is the position in the interaction region at which the NO scatters, $\mathbf{v}_p$ is the velocity of the product NO in the c.m. frame, $t$ is time, $t_s$ is the time that the scattering occurs, and $t_L$ is the time when the laser fires. The velocity of the product NO in the lab frame is given by $\mathbf{v}_p + \mathbf{v}_{\text{c.m.}}$. The quantities in the integrand are: $N_{\text{MB}}$ the intensity dependence of the two molecular beams, $I_L$, the intensity dependence of the laser, $\partial\sigma/\partial\Omega$, the differential cross section, and $f_t$, a function that relates the position of a detected ion in the image plane to its position and velocity after being ionized. For ideal velocity mapping, $f_t$ can be written:

$$f_t(\mathbf{v}, \mathbf{x}, \mathbf{x}_{\text{im}}) \cong \delta(v_\parallel - M\mathbf{x}_{\text{im}}) f_{\text{Jac}}(\mathbf{v}: \{\mathbf{v}_\parallel = M\mathbf{x}_{\text{im}}\}), \quad (2)$$

$$\text{where } \mathbf{v}_\parallel = \mathbf{v} - (\mathbf{v} \cdot \mathbf{n}_{\text{det}})\mathbf{n}_{\text{det}},$$

where $M$ is the magnification factor of ion lenses in m/s/mm, $\mathbf{n}_{\text{det}}$ is a unit normal vector perpendicular to the image plane, and $f_{\text{Jac}}$ is the Jacobian for the overlap of the three-dimensional scattering sphere onto the 2D detector. Initially, images were simulated using a Monte Carlo technique while manually iterating the input differential cross section until the appearance of the data and simulated images matched. However, utilizing some of the constraints of the system it is possible to construct a much faster image simulation algorithm that reproduces the main features of the apparatus function using numerical integration.[35]

The development of the numerical integration method depends on a few additional assumptions and a subsequent re-writing of the integral given by Eq. (1). The first assumption is that the molecular beam intensity function can be written as

$$N_{\text{MB}}(v_1, v_2, \mathbf{x}_p, t) = I_{\text{MB,vel}}(v_1, v_2) I_{\text{MB},t}(t) \mathbf{I}_{\text{MB,pos}}(\mathbf{x}_p), \quad (3)$$

where $I_{\text{MB,vel}}$ is the velocity dependence of the beam intensity, $I_{\text{MB,time}}$ is the time dependence of the beam intensity, and $I_{\text{MB,pos}}$ is the spatial dependence of the beam intensity. The time and velocity dependencies of the beams are assumed to be Gaussian. Furthermore, the beam spatial dependence is assumed to be constant within a cone determined by the molecular beam apertures. These assumptions allow $I_{\text{MB,vel}}$ to be extracted from the integral over $v_1$ and $v_2$. The assumption that $f_t$ can be written as a product of a delta function and $f_{\text{Jac}}$ combined with the energy constraints of the experiment for a given $v_1$ and $v_2$ (they are fixed because they are in the outer integral, which fixes the collision energy, $\mathbf{E}_{\text{coll}}$, and $\Delta E$ is fixed by $\Delta J$) allows the determination of the projection of $\mathbf{v}_p$ onto the detector plane. This fixes the full vector $\mathbf{v}_p$ to one of two vectors: one with a positive component along the TOF axis (perpendicular to the detector plane) and one with a negative component along the TOF axis. Thus, for a given pixel (the integral is written as a function of $x_I$), the integral over $\mathbf{v}_p$ can be replaced by a sum over these two possible vectors. The final assumption is that only NO present in the laser ionization volume when the laser fires need to be accounted for by the numerical integration, and that the sum over $\mathbf{v}_p$ can be removed from the integral over the scattering volume. This reduces the integral over the entire scattering volume to an integration over the laser ionization volume and an integration backwards in time to compute the amount of NO scattered with $\mathbf{v}_p$ into the laser ionization volume at the time when the laser fires. Furthermore, because the spatial density of the molecular beams is assumed to be constant within their defining cones, this backward integral in time can be performed analytically, given that the time dependence of the molecular beams is assumed to be Gaussian. The limits of integration $(t_1, t_2)$ for the time integral can be found from the geometric overlap of the NO trajectory with the molecular beam cylinders. With these assumptions and simplifications, Eq. (1) can be expressed as

$$I(x_1) = \int_{\text{molec}} \int_{\text{beam}} dv_1\, dv_2\, N_{\text{MB,vel}}(v_1, v_2) \times g \sum_1^2 \frac{\partial \sigma}{\partial \Omega} f_{\text{Jac}}(\mathbf{v}_{p,i}) \int_{\text{laser vol}} d\mathbf{x}_L\, I_L(\mathbf{x}_L) \int_{t_1}^{t_2} dt \times N_{\text{MB,time}}, (t) \quad (4)$$

where $\mathbf{v}_{p,i}\,(i = 1,2)$ are the two possible velocities of the product NO given a projection in the detector plane, and the remainder of the quantities in this expression are as defined previously. Using this algorithm for image simulation allows the computation of a simulated image orders of magnitude faster than the Monte Carlo method.

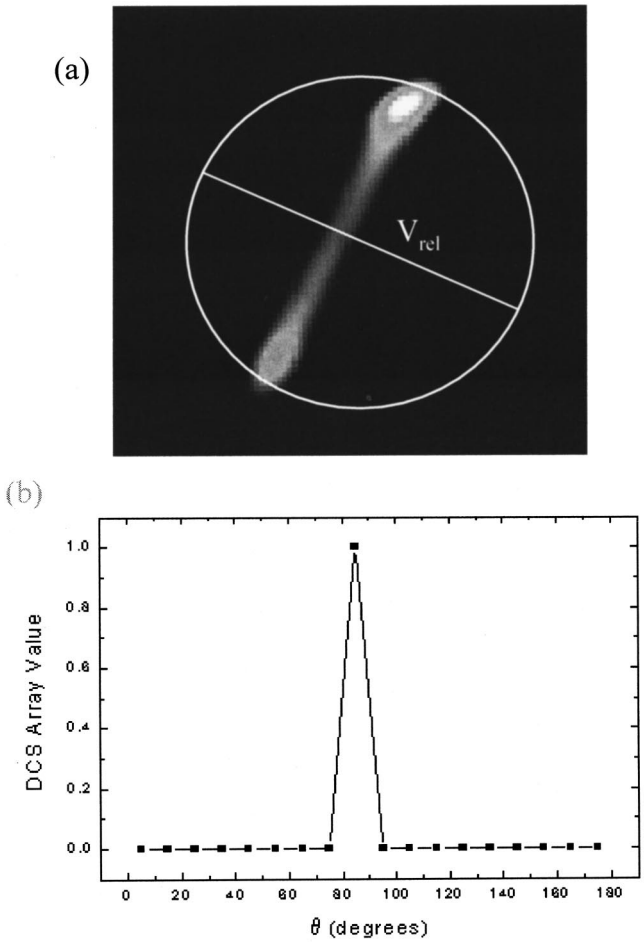


FIG. 5. (a) Basis image for an angular spike at 85°. (b) Input angular distribution for basis image.

### D. Extraction of the differential cross section

Rather than running the image simulation program for each trial differential cross section in an iterative image simulation process, it is possible to generate a set of nonorthogonal basis images from which a simulated image can be constructed. The differential cross section is input into the simulation program as an array of points (the DCS array), which represent the differential cross section at discrete values of $\theta$. Simulated images are a linear superposition of a set of basis images that correspond to a unit value input for each discrete $\theta$ value (and zero for all other $\theta$ values) in the DCS array. Figure 5 shows an example of the angular distribution and appearance of a basis image. By weighting these basis images with the trial DCS values and summing them, simulated images for the same set of experimental parameters but different trial DCS arrays can be generated almost instantaneously. This makes the process of iterative simulation quite fast. It is also possible to linearize the differential cross-section extraction process by evaluating the overlap of the basis images with the data images. This results in a system of linear equations that can be solved using matrix inversion algorithms. However, because the image inversion process is not unique (rapid oscillations added to a trial DCS array do not change a simulated image due to the various blurring effects) this linearization and inversion process are difficult.

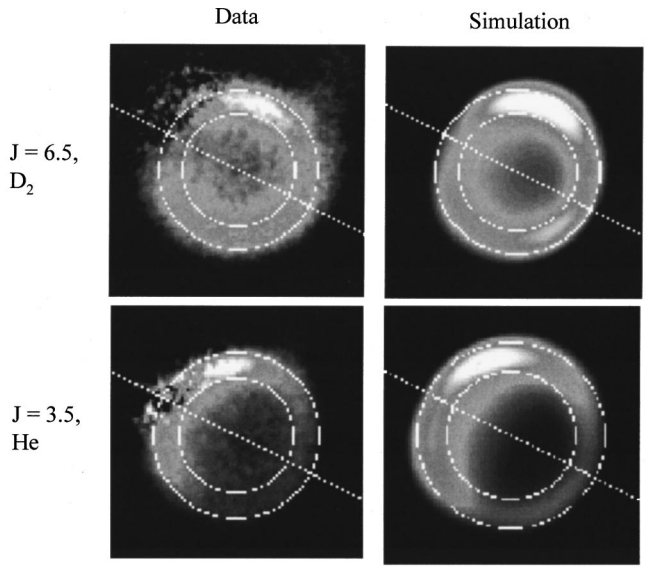


FIG. 6. Two examples of data and simulation fits. The dashed lines indicate the annular regions used to compare the two images for fitting.

Also, for this technique to work well, the simulated and data images must have their relative pixel sizes and positions extremely well matched. An iterative extraction technique is effective at producing a simulated image that is a close match to the data image.

The process of iteratively varying the trial DCS array to produce a simulated image that matches that data image has been described in detail in a previous article.[28] The process extracts a trial DCS array from the image from an annular integral of the outer edge of the scattering sphere, which strongly corresponds to the angular dependence of the differential cross section, but is skewed and blurred by the apparatus function. Figure 6 shows a typical annular integral used for the iterative fitting procedure. A simulated image with an isotropic differential cross section is generated, and the annular integral of this image is used as a first-order correction to the annular angular function from the data image. This first-order corrected DCS array is then used to produce a simulated image, which is used to produce a higher order correction to the trial DCS array. This process is repeated until the data and simulated images (their annular integrals) converge. The simulated images for several scattering measurements are shown in Fig. 6. In order to modify experimental parameters (such as the position of the laser ionization volume relative to the molecular beam intersection point), it is necessary to run the image simulation program to generate a new set of basis images. Independent measurements of all the experimental parameters, including laser position and laser ionization volume, were performed. The iterative fitting procedure gives an internal check on these parameters, because it has been found to not converge when there is a significant error in values of the experimental parameters. For example, the relative skewing of ion intensity about $\mathbf{v}_{rel}$ is not correctly modeled unless the left/right position of the laser is correct. Due to the sensitive nature of the goodness of fit on experimental parameters, the differential

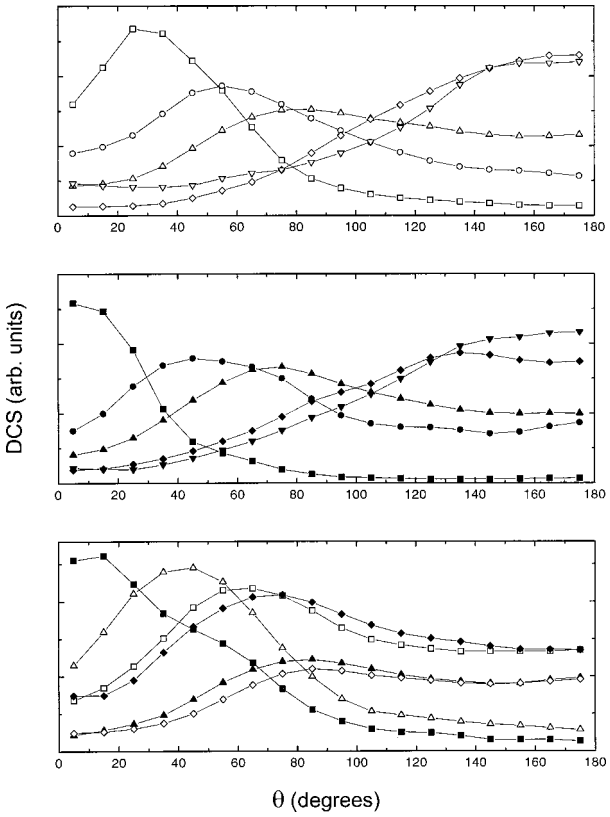


FIG. 7. Extracted differential cross sections for $F_1 \rightarrow F_1$ scattering. Open symbols are for He, while closed symbols are for $D_2$. In the top two panels, squares are for $J_f = 2.5$, circles for $J_f = 5.5$, triangles for $J_f = 7.5$, diamonds for $J_f = 9.5$, and inverted triangles for $J_f = 11.5$. In the bottom panel, squares are for $J_f = 3.5$, triangles for $J_f = 6.5$, and diamonds for $J_f = 8.5$.

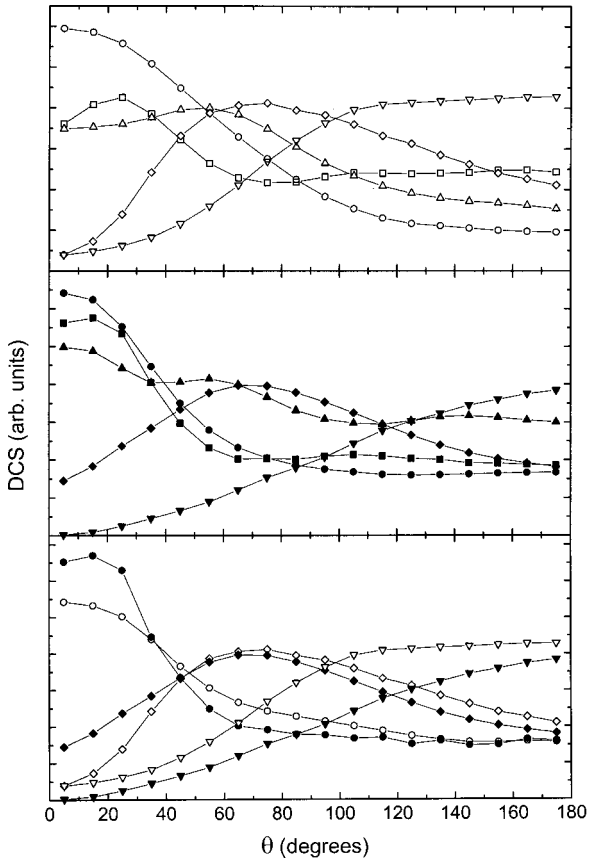


FIG. 8. Extracted differential cross sections for $F_1 \rightarrow F_2$ scattering. Open symbols are for He, while closed symbols are for $D_2$. In the top two panels, squares are for $J_f = 1.5$, circles for $J_f = 3.5$, triangles for $J_f = 4.5$, diamonds for $J_f = 6.5$, and inverted triangles for $J_f = 9.5$. In the bottom panel, circles are for $J_f = 2.5$, diamonds for $J_f = 6.5$, and inverted triangles for $J_f = 9.5$.

cross sections extracted using the above-given method are assumed to be accurate.

Plots of the extracted DCS arrays for the inelastic scattering of NO with He and $D_2$ from $J_i = 0.5$, $F_1$ to $J_f = 2.5-12.5$, $F_1$ are contained in Fig. 7. The top panel contains extracted DCSs for collisions of NO with He at a mean collision energy of 491 $cm^{-1}$. The middle panel displays selected DCSs extracted from NO/$D_2$ images with a mean collision energy of 545 $cm^{-1}$. The bottom panel shows a direct comparison of He and $D_2$ scattering for selected product rotational states. The NO scattering from $D_2$ is seen to be generally more forward peaked, with a narrower distribution, than the He scattered NO.

An error analysis of the images implies that the largest errors, approximately 15%, are associated with the forward scattered region. This is due to the interference of the NO in the molecular beam creating a ''beam spot'' on the images near the zero, or forward, deflection angle. The error limits for angles greater than 40° are generally believed to be less than 5%. The estimated error represents the propagation of counting error (the number of ions for a given intensity was estimated from the raw data images) of the subtracted image data through the iterative simulation process discussed previously. Errors in the simulation parameters were assumed to be minimal and were not treated in the error analysis.

Plots of the extracted DCS arrays for the inelastic scattering of NO with He and $D_2$ from $J_i = 0.5$, $F_1$ to $J_f = 1.5-9.5$, $F_2$ are shown in Fig. 8. The top panel displays the extracted DCSs for NO scattering with He. The middle panel shows the DCSs for NO/$D_2$ scattering and the bottom panel shows a direct comparison of He and $D_2$ scattering for several selected rotational product states. Note that in contrast with the spin–orbit conserving collisions, Fig. 7, there is seemingly little difference in the positions of the rainbow maxima between He and $D_2$ scattering for a given $J_f$ for the spin–orbit changing collisions. It is also seen that the positions of the rainbow peak are, to first order, independent of the spin–orbit state for a given $J_f$.

In general, the differential cross sections exhibit a broad rainbow maximum that monotonically shifts from the forward to backward scattering direction with increasing $\Delta J$. This is consistent with scattering systems where the repulsive surface of the potential controls the scattering behavior and can be well modeled by purely repulsive potentials. We use one such potential, a 2D hard ellipse potential, to model the differential cross section as will be discussed in detail in the following.

## IV. DISCUSSION

We have obtained differential cross sections for most of the available product rotational states for NO scattering from He and $D_2$, measured for both spin–orbit conserving and

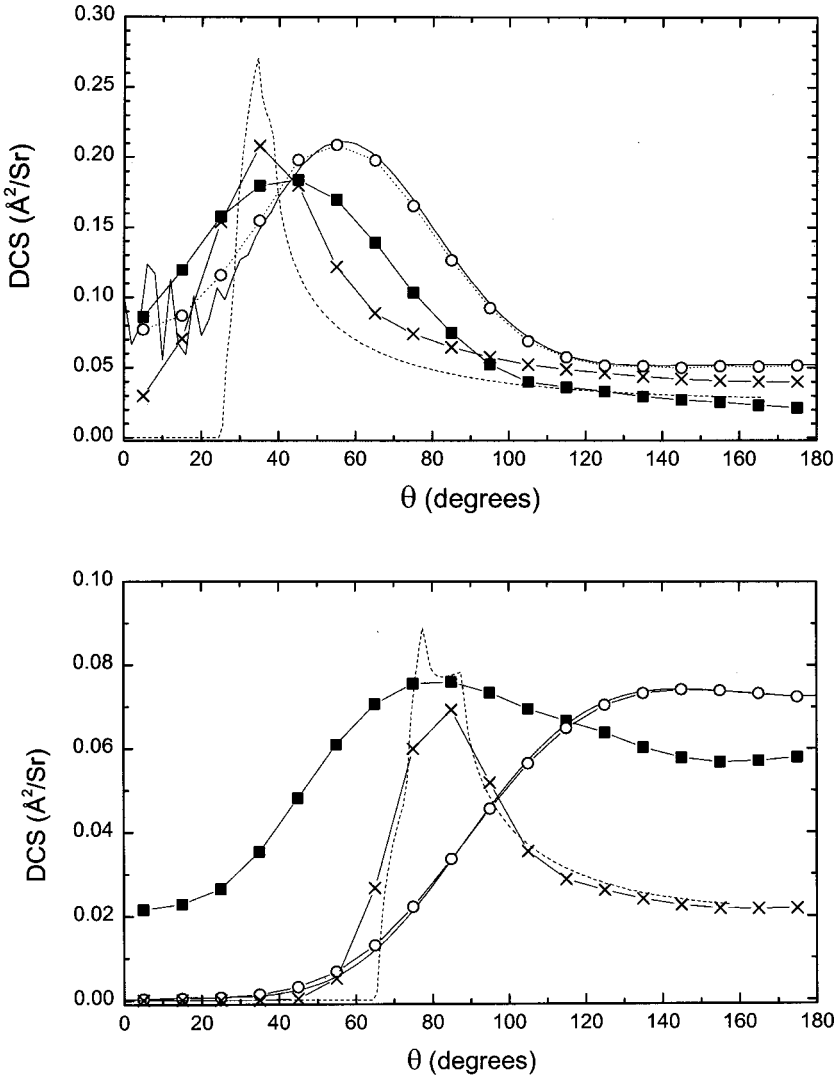


FIG. 9. Comparison of spin–orbit conserving differential cross sections between data, Yang–Alexander PES, and ellipse models for two $J_f$ levels. The model data have been used to simulate an image, then processed in the same way as the data to produce the model plots. In the top panel, the solid squares are experimental results for He and $J=3.5$, the solid line is the Yang–Alexander PES prediction, the open circles are a simulation based on the prediction of the Yang–Alexander surface, the dashed line is the prediction of a hard ellipse model, and the×symbols are the simulation based on the prediction of the hard ellipse model. In the bottom panel, the symbols have the same meaning as in the top panel, except that the data are for He and $J=7.5$.

spin–orbit changing collisions. The general behavior of the two systems is strikingly similar, indicating that the interaction potentials are also similar since the reduced masses of these two systems are identical. The more forward peaking of the $D_2$ system correlates with the higher collision energy for this system, however as we will show in the following, a portion of this effect may be attributed to a higher anisotropy in the repulsive wall of the NO/$D_2$ potential relative to that of the NO/He potential.

In order to interpret the data, two models have been used. The CEPA PES for NO+He of Yang and Alexander has been used to generate theoretical differential cross sections, which are then compared to experiment.[24] This PES is found to accurately reproduce the major features of the experimental data for NO+He with deviations in the positions of rainbow maxima. Due to the small differences between the differential cross sections for He and $D_2$, the NO+He PES also does a reasonable job predicting the angular distributions for scattering of NO+$D_2$, suggesting that this PES could be used to estimate NO+$D_2$ scattering measurements. Additionally, due to the seemingly simple behavior of the differential cross section as a function of $\Delta J$ and scattering species, a two-dimensional hard ellipse model was used to predict the scattering behavior for $F_1 \rightarrow F_1$ scattering. In general, by adjusting the anisotropy of the ellipse, the predicted rainbow maxima positions could be made to agree with the rainbow maxima from the data.

The most recent theoretical PES for NO+He scattering by Yang and Alexander has been used to produce theoretical differential cross sections using the numerical package entitled HIBRIDON. HIBRIDON is a package of programs for the time-independent quantum treatment of inelastic collisions and photodissociation written by Alexander *et al.*[36,37] The NO was assumed to have an initial population of 0.92 in $J=0.5$, $F_1$ and 0.08 in $J=1.5$, $F_1$ with an equal distribution between $\Lambda$ doublet states. The $\Lambda$ doublet state of the scattered NO was fixed by the transition used to ionize the NO (see Sec. II). NO+He collisions were simulated at collision energies of 491 and 545 $cm^{-1}$. A comparison of the experimental differential cross sections with calculated cross sections from the Yang and Alexander (YA) PES and a hard ellipse model (details are provided in the following) for selected spin–orbit conserving collisions is presented in Fig. 9. The experimentally extracted NO/He DCSs for $J_f=3.5$ (top panel) and $J_f=7.5$ (lower panel) are compared to the calculated YA DCSs and to DCSs extracted from images that

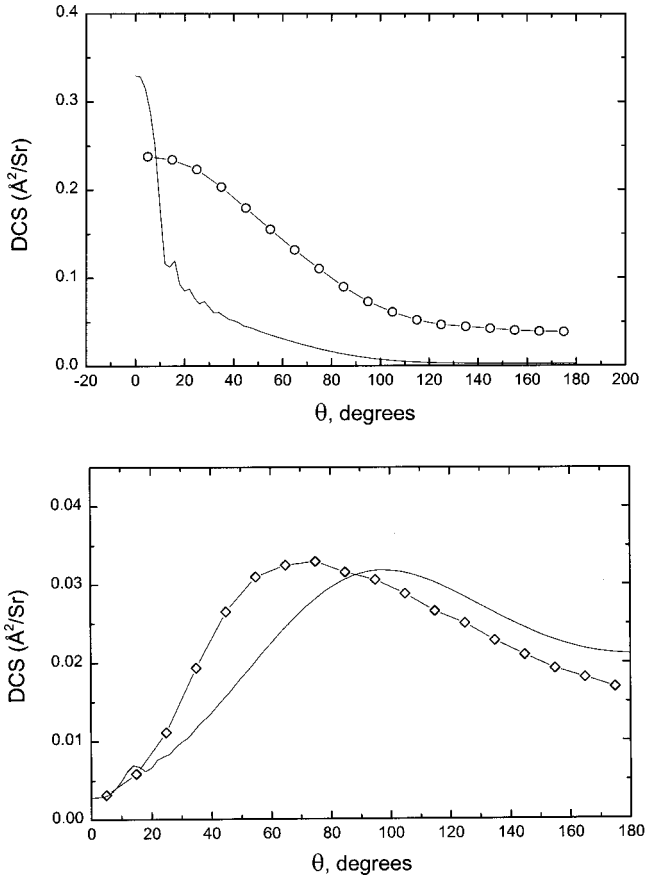


FIG. 10. Comparison of spin–orbit changing differential cross sections between data and Yang–Alexander PES for two $J_f$ levels. In the top panel, the open circles are for He and $J=3.5$, whereas the solid line is the prediction of the Yang–Alexander PES. In the bottom panel, the open diamonds are for He and $J=6.5$, whereas the solid line is the prediction of the Yang–Alexander PES.

have been simulated using the calculated YA DCSs as trial input cross sections. This simulation/extraction method is used in order to account for any distorting factors due to the extraction technique itself. The simulation/extraction DCSs are shown as open circles in Fig. 9. Note that the input YA PES DCS (solid line) and extracted DCS (open circles) are very similar, a fact which highlights the goodness of our extraction technique. While the general shape of the DCS calculated from the YA PES is similar to the experimental DCS (solid squares), the calculated distributions are positioned significantly toward higher deflection angles. This discrepancy could be accounted for by insufficient anisotropy in the repulsive wall of the YA PES. With insufficient anisotropy, collisions lack the necessary torque to promote rotational excitation. Therefore, a more nearly head-on collision, generating a larger deflection angle, is necessary to produce the needed change in angular momentum. The hard ellipse DCSs shown in the dashed lines of Fig. 9 will be discussed in the following.

Figure 10 shows experimental and calculated DCSs of two product states for spin–orbit changing collisions of the NO/He system. The theoretical DCSs have been extracted from simulated images using input DCSs obtained from calculations using the YA PES. Consistent with the spin–orbit conserving collisions shown in Fig. 9, the bottom panel shows that for $J_f=6.5F_2$, the theoretical DCS is peaked toward a higher scattering angle than the experimental DCS. For $J_f=3.5F_2$ (top panel) both the experimental DCS and that obtained from the YA PES peak at $\theta=0$ (forward scattering). However, the width of the scattering distribution is markedly broader in the experimental DCS. It is difficult to attribute this difference to a specific part of the YA PES.

The two-dimensional hard ellipse model has been shown to accurately reproduce maxima in rotationally inelastic scattering angular distributions, known as rotational rainbows.[38–40] The basic premise of the model is that the potential energy surface for the interaction can be replaced by a two-dimensional potential surface that has an infinitely high potential step on an elliptical contour. The shape of the ellipse can be estimated from the classical turning points of other potential surfaces. The rainbow maxima, for a given amount of rotational energy transfer, arise from the functional form of the deflection angle versus impact parameter and ellipse orientation angle for the collision. For a homonuclear, 2D ellipse model, with $\epsilon=\mu/I\ll 1$, the rainbow maxima can be approximated as

$$\sin\frac{1}{2}\theta_R=\frac{\Delta j}{2(A-B)}, \tag{5}$$

where $\theta_R$ is the rainbow angle, $\Delta j=j/p_0$, $j$ is the final angular momentum of the rotor, $p_0$ is the initial linear momentum, and $A$ and $B$ are the major and minor axes of the ellipse. For the systems studied here, $\epsilon=0.35$ Å$^{-2}$, so the results of this formula will probably be somewhat inaccurate. Furthermore, for a heteronuclear molecule, the center of mass of the ellipse is shifted from the geometric center of the ellipse by an amount $\delta$. This shift gives rise to two rotational rainbows for scattering from each end of the ellipse. For NO, $\delta$ is small, on the order of 0.05–0.10 Å, so NO can be considered almost a homonuclear molecule, and thus not much additional error is caused by use of the above-mentioned formula.

To simulate more rigorously the hard ellipse model for the case of NO+He/$D_2$, $F_1\rightarrow F_1$, it is possible to simulate the differential cross sections for the scattering process using the formula for scattering angle as a function of effective impact parameter, $\Delta j$ and $\epsilon$ from Bosanac and Buck:[39]

$$\sin\theta=\frac{\Delta j}{2b_n^2}\left[\frac{4b_n^2-(\Delta j)^2(1+\epsilon b_n^2)^2}{1-\epsilon(\Delta j)^2}\right]^{1/2}, \tag{6}$$

where $b_n$ is the effective impact parameter which can be calculated from the appropriate geometric equations for a range of impact parameters and ellipse orientations. By integrating over impact parameter and ellipse orientation, and storing the results as a function of $\Delta j$ and scattering angle, $\theta$, model hard ellipse DCS and corresponding rainbow maxima, $\theta_R$, can be generated for different rotational product states. For heteronuclear molecules the center of mass is displaced from the geometrical center of the ellipse, giving rise to two unique rainbow maxima. Due to the near homonuclear character of NO and the experimental resolution limits, it is not possible to resolve these two rainbow maxima—even in the

model calculation. Figure 9 shows 2D hard ellipse DCSs for NO/He scattering for $J_f = 3.5$ and 7.5 (dashed lines). Note that the DCSs rise from zero in the classically forbidden region to a maximum at the classical rainbow, and then fall off toward higher scattering angles. The position of the maximum is determined solely by the collision energy and the relative sizes of the semimajor and semiminor ellipse axes $A$ and $B$, respectively. Also included are extractions of the DCSs from simulated images using these hard ellipse DCSs as inputs (line connecting×symbols). The extracted DCSs are broadened due to the limited resolution in the experiment, due primarily to the velocity spread in the molecular beams. This effect is especially pronounced in the forward scattering region, and is compounded by the addition of a background ''beam spot.''

By adjustment of the ellipse parameters, especially the anisotropy $(A-B)$, the rainbow maxima positions of the extracted DCSs for the rotational states for each of the NO+He and NO+$D_2$ collision systems can be fit to a relatively simple hard ellipse model. Figure 11 shows a comparison of rainbow maxima, $\theta_R$, extracted from calculated DCSs using the YA PES, and those taken from the experimentally extracted DCSs, as well as a fit to the experimental rainbow positions. Data for $J = 9.5-10.5$ have not been included in the fit because (1) the data do not conclusively show whether there is a peak in the angular distribution or whether the data are simply backscattered, and (2) there is an intrinsic uncertainty in the extraction procedure that makes the nearly backscattered peak positions very sensitive to the assumed position of the laser beam. Note that the rainbow maximum angles calculated using HIBRIDON and the YA PES are consistently higher than the measured rainbow maxima. This is true for both the He (triangles) and the $D_2$ (crosses) scattering. For NO+He ($F_1 \rightarrow F_1$), the results of fitting the observed rainbow maxima positions to a 2D hard ellipse model (solid line fit to closed circles) give results of $(A-B) = 0.62$ Å and $\delta = 0.04$ Å (using $A \approx 2.7-3.1$ Å). It is not possible to fit a value of $\delta$ with much certainty due to the lack of resolution of the two rotational rainbow peaks. The results for NO+$D_2$ ($F_1 \rightarrow F_1$) are similar (dashed line fit to open squares), but with noticeably higher anisotropy: $(A-B) = 0.76$ Å and $d = 0.14$ Å (using $A \approx 2.7-3.1$ Å). These model ellipse anisotropies can be compared to estimates of the anisotropy in the repulsive wall of the CEPA PES of Yang and Alexander. The YA PES contours near 500 $cm^{-1}$ (comparable to the collision energy of our experiment) give values for $A$ and $B$ of ~2.8 and ~2.4 Å, respectively. This results in a value of $(A-B) = 0.4$ Å, which is considerably less than the anisotropy given by the 2D hard ellipse models extracted from either the NO/He or NO/$D_2$ data presented in this study. A lower repulsive anisotropy will result in scattering distributions that are positioned at higher deflection angles. This trend is shown in Fig. 11. Note that the rainbow positions, derived from the YA DCSs, are positioned to higher deflection angles relative to the 2D hard ellipse rainbows for all J values. In addition, the value of the YA theoretical $\theta_R$ rises more rapidly with $J_f$ than either of the hard ellipse models, to the point that there may not be sufficient anisotropy for reaching the collisional energetic limit. This observation is born out by CS calculations of integral cross sections, which show that at a collision energy of 508 $cm^{-1}$ the best value of $J_{max}$ is about 11.5, corresponding to a rotational energy of 240 $cm^{-1}$.[24]

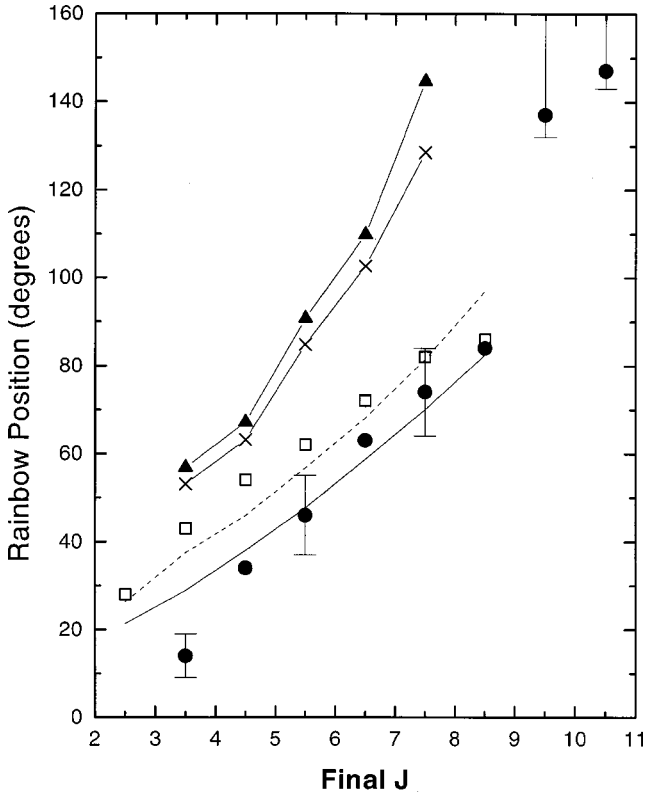


FIG. 11. Plot of rainbow maxima vs $J_f$ for data, the Yang–Alexander PES, and the hard ellipse models. Closed circles are data for $D_2$/NO; open squares are data for He/NO; solid and dashed lines are fits to a hard-ellipse model for the $D_2$ and He data, respectively (see the text); triangles and crosses are HIBRIDON predictions for He/NO at collision energies of 491 and 545 $cm^{-1}$, respectively.

As a final comparison between the theoretical predictions for the differential cross section and the DCSs extracted from the experimental data, it is possible to use the theoretical differential cross sections to produce simulated images to compare directly with the raw data images. The results of these comparisons illustrate the limitations in measuring the differential cross section for the most forward scattered products due to the interference with the beam spot. Furthermore, while the hard ellipse calculations are successful in fitting the rainbow maxima of the data reasonably well, the PES of Yang and Alexander naturally predicts more accurately the broadness of the rainbow peaks, because quantum mechanics eliminates the singularities encountered in classical scattering differential cross sections. We therefore conclude that a fully quantum mechanical calculation using a repulsive surface with an anisotropy similar to that which we find using the hard ellipse fit should be in excellent agreement with the differential cross sections presented here.

## V. SUMMARY

Differential cross sections for rotationally inelastic scattering of NO with He and $D_2$ at ~500 $cm^{-1}$ collision energy

have been measured using crossed molecular beam ion imaging and extracted using a new forward simulation basis image technique. The positions of the rainbow peaks obtained from the extracted differential cross sections for $J_f < 9.5$ are found to be well fit by a hard ellipse model. This model underestimates the broadness of the rainbow peaks. The differential cross sections obtained using the Yang and Alexander PES are typically more backward scattered than the data, indicating that the anisotropy of the repulsive wall of their potential may be too low. The data for $J_f > 9.5$ show a larger change in the rainbow scattering angle than is predicted by extrapolation of the low-$J$ hard ellipse model. The high-$J_f$ peak positions are in closer agreement with the positions calculated by Yang and Alexander.

For spin–orbit conserving collisions, the NO scattered from $D_2$ is seen to be more forward scattered than the NO scattered from He. The differences in the differential cross sections between NO+He and NO+$D_2$ are small and are partially, but not totally, attributable to the higher collision energy of the NO+$D_2$ system. Only small differences are observed between the rainbow positions of the spin–orbit changing and spin–orbit conserving collisions.

## ACKNOWLEDGMENTS

The authors gratefully acknowledge the assistance of A. Dixit and P. J. Pisano in collecting the spin multiplet changing images from the apparatus at Cornell University. The work at Cornell was supported by the Department of Energy, Basic Energy Sciences, under Grant No. DE-FG02-88ER13934. The work at Sandia was supported by the U.S. Department of Energy, Office of Basic Energy Sciences, Department of Chemical Sciences.

[1] A. S. Sudbo and M. M. T. Loy, Chem. Phys. Lett. **82**, 135 (1981).
[2] A. S. Sudbo and M. M. T. Loy, J. Chem. Phys. **76**, 3646 (1982).
[3] M. Islam, I. W. M. Smith, and M. H. Alexander, Chem. Phys. Lett. **305**, 311 (1999).
[4] P. L. James, I. R. Sims, I. W. M. Smith, M. H. Alexander, and M. Yang, J. Chem. Phys. **109**, 3882 (1998).
[5] H. Joswig, P. Andresen, and R. Schinke, J. Chem. Phys. **85**, 1904 (1986).
[6] M. H. Alexander, J. Chem. Phys. **99**, 7725 (1993).
[7] S. D. Jons, J. E. Shirley, M. T. Vonk, C. F. Giese, and W. R. Gentry, J. Chem. Phys. **97**, 7831 (1992).
[8] J. Troe, J. Chem. Phys. **66**, 4745 (1977).
[9] A. Lin, S. Antonova, A. P. Tsakotellis, and G. C. McBane, J. Phys. Chem. A **103**, 1198 (1999).
[10] S. D. Jons, J. E. Shirley, M. T. Vonk, C. F. Giese, and W. R. Gentry, J. Chem. Phys. **105**, 5397 (1996).
[11] M. Keil, J. T. Slankas, and A. Kuppermann, J. Chem. Phys. **70**, 541 (1979).
[12] H. Thuis, S. Stolte, and J. Reuss, Chem. Phys. **43**, 351 (1979).
[13] H. H. W. Thuis, S. Stolte, J. Reuss, J. J. H. van den Biesen, and C. J. N. van den Meijdenberg, Chem. Phys. **52**, 211 (1980).
[14] J. A. Bacon, C. F. Giese, and W. R. Gentry, J. Chem. Phys. **108**, 3127 (1998).
[15] M. T. Vonk, J. A. Bacon, C. F. Giese, and W. R. Gentry, J. Chem. Phys. **106**, 1353 (1997).
[16] M. Drabbels, A. M. Wodtke, M. Yang, and M. H. Alexander, J. Phys. Chem. A **101**, 6463 (1997).
[17] H. Meyer, J. Chem. Phys. **102**, 3151 (1995).
[18] T. Orlikowski and M. H. Alexander, J. Chem. Phys. **80**, 4133 (1984).
[19] V. Khare, D. J. Kouri, and D. K. Hoffman, J. Chem. Phys. **74**, 2656 (1981).
[20] V. Khare, D. J. Kouri, and D. K. Hoffman, J. Chem. Phys. **74**, 2275 (1981).
[21] H. Meyer, Chem. Phys. Lett. **230**, 519 (1994).
[22] G. C. Nielson, G. A. Parker, and R. T. Pack, J. Chem. Phys. **66**, 1396 (1977).
[23] M. H. Alexander and T. Orlikowski, J. Chem. Phys. **80**, 1506 (1984).
[24] M. Yang and M. H. Alexander, J. Chem. Phys. **103**, 6973 (1995).
[25] L. S. Bontuyan, A. G. Suits, P. L. Houston, and B. J. Whitaker, J. Phys. Chem. **97**, 6342 (1993).
[26] A. G. Suits, L. S. Bontuyan, P. L. Houston, and B. J. Whitaker, J. Chem. Phys. **96**, 8618 (1992).
[27] N. Yonekura, C. Gebauer, H. Kohguchi, and T. Suzuki, Rev. Sci. Instrum. **70**, 3265 (1999).
[28] K. T. Lorenz, M. S. Westley, and D. W. Chandler, Phys. Chem. Chem. Phys. **2**, 481 (2000).
[29] K. T. Lorenz, D. W. Chandler, and G. C. McBane (unpublished).
[30] A. T. J. B. Eppink and D. H. Parker, Rev. Sci. Instrum. **68**, 3477 (1997).
[31] M. S. Westley, Ph.D. thesis, Cornell University, Ithaca, NY, 2000.
[32] E. E. Marinero, C. T. Rettner, and R. N. Zare, Phys. Rev. Lett. **48**, 1323 (1982).
[33] K. D. Rinnen, M. A. Buntine, D. A. V. Kliner, R. N. Zare, and W. M. Huo, J. Chem. Phys. **95**, 214 (1991).
[34] M. H. Alexander *et al.*, J. Chem. Phys. **89**, 1749 (1988).
[35] G. C. McBane (unpublished).
[36] M. H. Alexander, D. E. Manolopoulus, H. J. Werner, and B. Follmeg, HIBRIDON 4.1 ed. (1996).
[37] M. H. Alexander and D. E. Manolopoulos, J. Chem. Phys. **86**, 2044 (1987).
[38] S. Bosanac, Phys. Rev. A **22**, 2617 (1980).
[39] S. Bosanac and U. Buck, Chem. Phys. Lett. **81**, 315 (1981).
[40] W. Schepper, U. Ross, and D. Beck, Z. Phys. A **290**, 131 (1979).